Materials and Design 194 (2020) 108968

Contents lists available at ScienceDirect

Materials and Design

journal homepage: www.elsevier.com/locate/matdes

Microstructurally flexible high entropy alloys: Linkages between alloy design and deformation behavior

S.S. Nene [a], M. Frank [a], P. Agrawal [a], S. Sinha [a], K. Liu [a], S. Shukla [a], R.S. Mishra [a,*], B.A. McWilliams [b], K.C. Cho [b]

[a] Center for Friction Stir Processing, Department of Materials Science and Engineering, University of North Texas, Denton, TX 76207, USA
[b] Weapons and Materials Research Directorate, CCDC Army Research Laboratory, Aberdeen Proving Grounds, MD 21005, USA

HIGHLIGHTS

- Metastability based alloy design led to flexible microstructural evolution in which either thermodynamically stable γ-phase or unstable ε-phase was obtained at room temperature.
- The main strain accommodation mechanism in γ phase is TRIP exhibiting S—N $((111)\gamma \parallel (0001)\varepsilon$ and $\left(10\bar{1}\right)\gamma \| \left(11\bar{2}0\right)\varepsilon)$ orientation relationship among γ/ε interfaces.
- Activation of non-basal activity assisted nano-plate formation at early stages and nano-twinning at later stages accommodated the deformation in ε phase.
- Flexibility-based design opened an uninvestigated compositional as well as mechanical property domain that is useful for higher flexibility in safe engineering design.

GRAPHICAL ABSTRACT

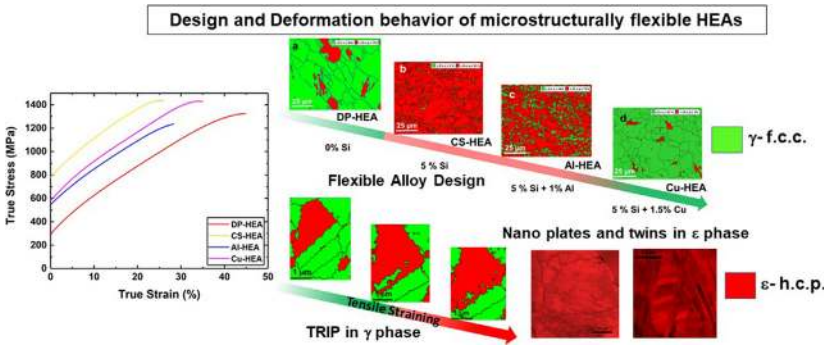

ARTICLE INFO

Article history:
Received 29 June 2020
Received in revised form 5 July 2020
Accepted 9 July 2020
Available online 14 July 2020

Keywords:
Microstructural flexibility
H.c.p. high entropy alloys
Nano twins
Nano plates
Transformation induced plasticity

ABSTRACT

Development of multicomponent alloys, popularly known as high entropy alloys (HEAs) provides abundant compositional space for designing a variety of HEAs, including equiatomic, dual phase and microstructurally flexible (MF-HEAs). Among them, the design of MF-HEAs further extends the HEA domain in terms of understanding adaptive phase evolution with respect to change in alloy chemistry and processing parameters. This responsive phase evolution enabled near single phase ε (h.c.p., 95%) or γ (f.c.c., 90%) dominant microstructures, depending on imposed processing strain, strain rate and temperature for a selected alloy chemistry. The γ-phase dominated HEAs showed slower yet sustained work hardening (WH) rates (~ 2000 MPa) owing to transformation induced plasticity (TRIP) effect whereas ε-phase dominated microstructure showed exceptionally high and sustained work hardening rates (2300–2700 MPa) due to formation of nano plates or twins in ε-phase upon deformation. Therefore, MF-HEA design leads to exceptional strength–ductility synergy (1100-1250 MPa, 30-43%) irrespective of the dominance of either γ- or ε-phase in the starting microstructure owing to selective operation of deformation mechanisms in the dominant phase.

* Corresponding author.
E-mail address: Rajiv.Mishra@unt.edu (R.S. Mishra).

https://doi.org/10.1016/j.matdes.2020.108968

1. Introduction

Conventional metals and alloys exhibit certain responses to the processing and heat treatments imposed on them in terms of microstructural evolution and subsequent deformation behavior. For example, certain steels or Al alloys show thermodynamic phase stability and slip-dominant plasticity as expected in FCC alloys [1,2]. Advances in alloy design strategies for incorporating different strengthening mechanisms such as precipitation, dispersion, transformation or twinning, along with slip has given rise to various advanced high-strength materials like precipitation hardened steels, transformation/twinning induced plasticity steels and deformed and portioned steels [1–3]. Recent work on the cold-worked and partitioned transformation induced plasticity (TRIP) steels showed exceptionally high yield strength (YS) with reasonably good ductility owing to the controlled TRIP effect during deformation [3].

A new alloy design approach that goes against the conventional development strategy of having a principal alloying element gave rise to the new class of materials termed "high-entropy alloys (HEAs)" or "complex concentrated alloys (CCAs)." The initial motivation behind this approach was to form a concentrated multi-element solid solution instead of forming intermetallic second phases in the material to attain massive solid solution strengthening [4–6]. Similar observations were made for the standard equiatomic CoCrFeMnNi HEA showing very high strength and ductility and cryogenic damage tolerance with single phase γ (f.c.c.) matrix [5–7]. Recently, researchers pointed out the importance of multiphase microstructures in HEAs that showed unconventional mechanical and fracture-resistant behavior at room temperature [8–11]. The best examples from this category are the $Al_xCoCrFeNi$ HEAs [8,9] and the recently-designed dual phase (DP) HEA ($Fe_{50}Mn_{30}Co_{10}Cr_{10}$) [10], which showed extensive twinning-induced plasticity (TWIP) and TRIP, respectively [8,10,11]. Moreover, the former showed extremely high corrosion resistance and fatigue strength [8,9], whereas the latter displayed exceptional ductility at room temperature [10,11].

Our recent work along similar lines of having multiphase multicomponent alloys by tuning the stability of the γ-phase resulted in not only exceptional mechanical properties but also responsive phase stability with respect to alloy chemistry, processing parameters and heat treatment times [12–15]. We termed this adaptive phase evolution as "microstructural flexibility." The present paper discusses the approach we used to realize "microstructurally flexible" HEAs along with a brief introduction to the concept of microstructural flexibility. Further, the effect of flexible microstructural engineering on deformation response for all these HEAs is discussed in detail and an overview comparison of the mechanical properties of these HEAs with steels and other HEAs is presented in brief.

2. Experimental

2.1. Materials and processing

All the HEAs were produced by vacuum arc-casting in a cold-copper crucible. The vacuum level achieved was approximately 300 μm (corresponds to mean free path for active gases), and the chamber was backfilled with argon to 1 atm prior to each melt, using pure metals and ingot dimensions of $300 \times 100 \times 6$ mm^3. The nominal compositions for all HEAs used in the present work are given in Table 1.

Table 1
Nomenclature of TRIP HEAs used in this work along with their nominal compositions.

HEA	Composition (all in at.%)
CS-HEA	$Fe_{40}Mn_{20}Co_{20}Cr_{15}Si_5$
Al-HEA	$Fe_{39}Mn_{20}Co_{20}Cr_{15}Si_5Al_1$
Cu-HEA	$Fe_{38.5}Mn_{20}Co_{20}Cr_{15}Si_5Cu_{1.5}$

2.2. Friction stir processing (FSP)

As-cast 6 mm thick sheets were then friction stir processed using a W—Re tool with the parameters shown in Table 2. Single pass processing was carried out at tool rotational rate of 350 rotations per minute (RPM). A Cu backing plate was used for effective heat dissipation, and Ar was blown near the specimen tool interface to avoid oxygen pickup during processing. The processing tool had a shoulder diameter of 12 mm with a tapered pin. The root diameter, pin diameter, and length of the tool were 7.5 mm, 6 mm, and 3.5 mm, respectively.

2.3. Microstructural characterization

Microstructures of the all the HEAs were analyzed by various methods. Electron backscatter diffraction (EBSD) measurements were carried out by an Field emssion based NOVA Nano (FE-SEM) with a Hikari camera, and the data were analyzed using TSL OIM 8 software. As the grain size attained during FSP was significantly fine, EBSD scans were done at two magnifications; i.e., 2000 X and 6000 X. To capture sufficient grains during higher magnification scans (6000 X), grain size and phase fractions were estimated at three different locations, and the average values have been reported. Step size and scan area for all conditions were 0.08 μm and 25×20 μm^2, respectively. Transmission electron microscopy (TEM) based orientation imaging microscopy (OIM) known as precession electron diffraction (PED) [16], was carried out to image the features on FEI Tecnai G2 F20 S-Twin 200 keV. For PED, the TEM foils were milled out using FEI Nova 200 NanoLab dual beam focused ion beam (FIB) FE-SEM. PED data was acquired using TOPSPIN 3.0 software and analyzed using ACOM software, both from NanoMEGAS.

2.4. Tensile testing and interrupted tensile tests

Rectangular 1 mm-thick, dog-bone-shaped mini-tensile specimens were machined using a computer numerical control (CNC) machine from 1 mm below the surface within the nugget region of all HEAs. Gage length and width of the tensile specimens pre deformation were 5 and 1.25 mm, respectively. For each condition, tensile tests were performed at room temperature and an initial strain rate of 10^{-3} s^{-1}. Three samples were tested to confirm reproducibility of the results.

For interrupted tensile tests, the specimen was deformed at 10^{-3} s^{-1} and the test was stopped after 5 and 7.5% strain, respectively. In order to capture same grains in EBSD scans post deformation, specimens were indented at three different locations on the gage of the mini-tensile specimen and the results shown in the current work are from the central region of gage section of the specimen. EBSD was carried out as explained in Section 2.4 without polishing the specimen after interruption.

3. Results and discussion

3.1. Microstructural flexibility

The concept of microstructural flexibility was achieved from tunable phase stability in a Fe-Mn-Co-Cr-Si HEA system, by changing the alloy chemistry and processing parameters (strain, strain rate and

Table 2
Processing parameters selected for FSP.

Processing parameters	S350
Rotational rate (RPM)	350
Traverse speed (mm/min)	50.8
Plunge depth (mm)	3.65
Tilt angle (°)	2.0

temperature) in synergy. Ni- or Co-dominant Si containing stainless steels were reported to have such a responsive phase evolution, which earlier work referred to as dynamic phase stabilization under extreme strain and temperature processing [17–19] Similarly, the ability to obtain different combination of either a thermodynamically stable γ (f.c.c) or unstable ε (h.c.p.) phase in the microstructure at room temperature under the combined effect of strain, strain rate, temperature and alloy chemistry is being termed as "microstructural flexibility". Earlier work on TRIP assisted steels confirmed that, formation of near single phase ε is difficult due to either higher stability of γ (austenite) or larger driving force for α' martensite formation [17–20]. However, in case of TRIP HEAs increased metastability of γ matrix lowers the barrier for ε formation in terms of required strain-temperature combination to trigger this transformation during processing at higher temperatures.

Fig. 1 (a-c) schematically presents the thermodynamic basis for the microstructural flexibility. It is known that metastable phase has an activation barrier to transform to stable phase at a given temperature and composition [20,21]. As we are considering the γ→ε transformation, ε-phase is taken as stable phase and γ-phase is treated as metastable phase having driving force of $\Delta G^{\gamma\rightarrow\varepsilon}$ J/mol for the γ → ε transformation in Fe-Mn-Co-Cr system (Fig. 1 (a)). This $\Delta G^{\gamma\rightarrow\varepsilon}$ can be increased to $\Delta G^{\gamma\rightarrow\varepsilon*}$ by addition of ε stabilizers to an amount $\Delta G^{\gamma\rightarrow\varepsilon\ (chem)}$ (Fig. 1 (b)), thereby increasing the γ metastability. If the same alloy with $\Delta G^{\gamma\rightarrow\varepsilon*}$ is strained at higher temperature, the stability of either phases at high temperature decides the resultant phase in the microstructure at room temperature (imposed strain increases the $\Delta G^{\gamma\rightarrow\varepsilon}$ further by the amount of $\Delta G^{\gamma\rightarrow\varepsilon\ (strain)}$ whereas temperature tries to reduce it by $\Delta G^{\gamma\rightarrow\varepsilon\ (temp)}$) as shown in Fig. 1 (c). Consider a case when strain dominates over temperature wherein $\Delta G^{\gamma\rightarrow\varepsilon\ (strain)} > \Delta G^{\gamma\rightarrow\varepsilon\ (Temp)}$ hold good and hence effectively increase the overall driving force to $\Delta G^{\gamma\rightarrow\varepsilon*} = (\Delta G^{\gamma\rightarrow\varepsilon\ (strain)} - (\Delta G^{\gamma\rightarrow\varepsilon\ (Temp)})) + \Delta G^{\gamma\rightarrow\varepsilon}$ and hence can stabilize thermodynamically unstable ε-phase at room temperature. However, for the reverse case where temperature dominates over strain ($\Delta G^{\gamma\rightarrow\varepsilon\ (Temp)} > \Delta G^{\gamma\rightarrow\varepsilon\ (strain)}$), overall driving force becomes small for ε formation and hence stabilizes thermodynamically stable γ-phase (Fig. 1 (d)). This argument suggests that if the Fe-Mn-Co-Cr system contains ε stabilizers, synergistic application of strain, strain rate an temperature can trigger either γ or ε-phase dominance in the microstructure which we called microstructural flexibility. This concept gave rise to the composition-processing-phase stability triangle (CPPT) as shown in Fig. 1 (e) which captures the responsive phase evolution in the material subjected to a particular processing schedule for a given alloy chemistry.

Fig. 2 (a_1-a_3) and (b_1-b_3) show the CPPT triangle for $Fe_{50}Mn_{30}Co_{10}Cr_{10}$ (DP-HEA) and $Fe_{40}Mn_{20}Co_{20}Cr_{15}Si_5$ (CS-HEA) after FSP at 350 RPM, respectively. It is clear from these figures that, under similar processing conditions, DP-HEA (Fig. 2 (a_3)) showed stabilization of γ-phase dominated microstructure whereas CS-HEA showed dominance of ε-phase in the microstructure. As the processing condition was same, the temperature and strain imposed were similar and hence difference in phase stability is due to presence of ε-phase stabilizer Si and Co in CS-HEA (Fig. 2 (b_3)). Thus, this observation suggests that CS-HEA can stabilize the thermodynamically unstable ε-phase at RT and hence is more flexible than DP-HEA. Moreover, flexibility assisted design faciliated formation of ε-phase dominated microstructure which was difficult in conventional steels and HEAs. Thus, the alloy design strategy that led to flexible alloy chemistry is illustrated in subsequent section.

3.2. Metastability based alloy design: path to microstructural flexibility

As discussed in the previous section, metastability provides higher probability of matrix phase transformation to product phase due to overall decrease in activation barrier for transformation (or increase in the driving force). Thus, the activation barrier for ε-phase formation can be lowered by increasing the probability of intrinsic stacking faults (i-SFs) in the microstructure. This is because the mechanism of ε-phase formation has been proposed to be associated with the successive layering of these i-SFs on consecutive [111] planes [22–24]. In other words, the activation barrier for ε formation can be tuned by effective

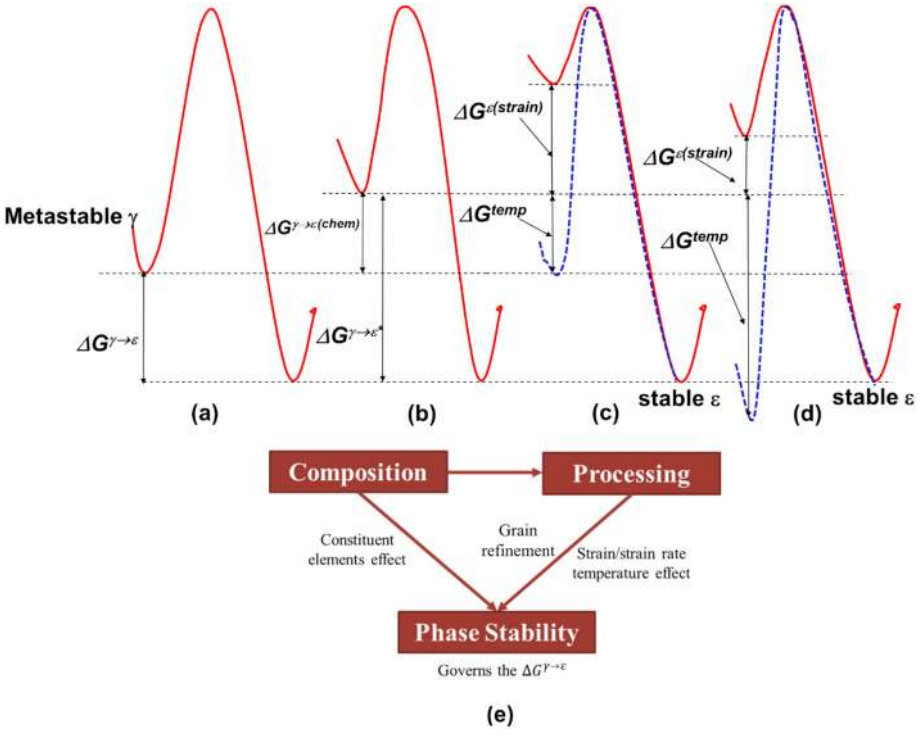

Fig. 1. (a-d) Schematic illustration of the thermodynamic basis for the microstructural flexibility. (e) The composition-processing-phase stability (CPPT) triangle to capture the effect of alloy chemistry, strain, strain rate and temperature on phase stability.

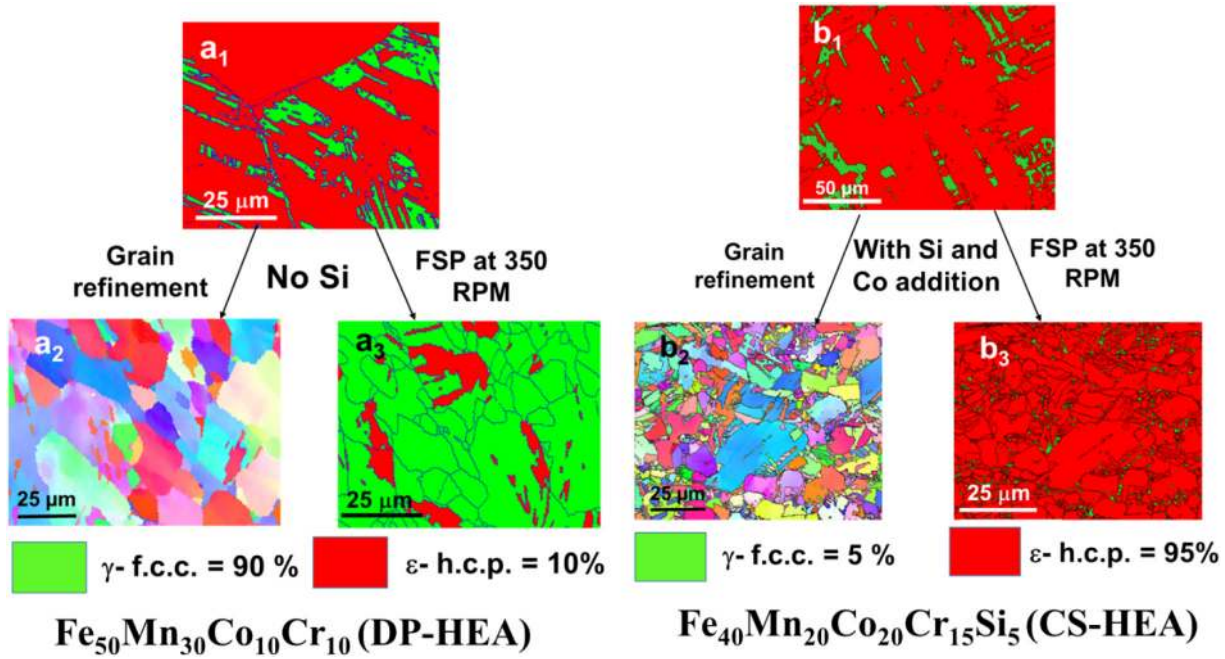

Fig. 2. Microstructural flexibility in TRIP HEAs. (a) The composition–processing-phase stability triangle illustrated with DP-HEA, (a_1) EBSD phase map in as-cast condition, (a_2) EBSD IPF map for S350 condition, and (a_3) EBSD phase map for S350 condition. (b) The composition –processing-phase stability triangle illustrated with CS-HEA, (b_1) EBSD phase map in as-cast condition, (b_2) EBSD IPF map for S350 condition, and (b_3) EBSD phase map for S350 condition. (EBSD: electron back scattered diffraction, HEA: high entropy alloy, TRIP: Transformation induced plasticity, IPF: inverse pole figure).

selection of alloy chemistry which can reduce stress required for dissociation of perfect dislocations into partials in the γ matrix to form stable intrinsic stacking faults (SFs). One of the ways to achieve this is the lowering of stacking fault energy (γ_{SFE}) of the alloy which can stabilize the SFs by maximizing the SF ribbon width. According to TRIP litertaure [22–24],

$$\gamma_{SFE} = n\rho\Delta G^{\gamma\to\varepsilon} + n\sigma^{\gamma/\varepsilon} \quad (1)$$

where γ_{SFE} is the stacking fault energy, ρ is the planar density of closed packed plane, $\Delta G^{\gamma\to\varepsilon}$ is the Gibb's free energy for γ → ε transformation and $\sigma^{\gamma/\varepsilon}$ is the interfacial energy between γ and ε phases. As the interfacial energy barrier in ε formation is lower due to coherency, $\Delta G^{\gamma\to\varepsilon}$ decides the overall γ_{SFE} and thus can be a tuning factor for engineering the metastability of γ-phase.

The $\Delta G^{\gamma\to\varepsilon}$ can be engineered by two ways: (a) variation in alloy chemistry in conventional alloy design, and/or (b) increasing the number of constituent elements while changing the chemistry as per high entropy approach. The high entropy approach is more effective since increasing the $\Delta S_{conf}^{\gamma\to\varepsilon}$ of the alloy system points towards increasing the probability of having more stable SFs which can help in ε-phase by increasing nucleation sites. Thermodynamically, $\Delta S_{conf}^{\gamma\to\varepsilon}$ affects the $\Delta G^{\gamma\to\varepsilon}$ as,

$$\Delta G^{\gamma\to\varepsilon} = \Delta H_{mix}^{\gamma\to\varepsilon} - T\Delta S_{conf}^{\gamma\to\varepsilon} \quad (2)$$

where $\Delta H_{mix}^{\gamma\to\varepsilon}$ is the enthalpy of mixing effect on the transformation.

According to Richard's rule [20] and Yeh et al. [4] consideration, increasing the number of constituent elements in the alloy increases the propensity for the formation of disordered solid solution [19–21]. Our design approach indirectly involves control of not only driving force for γ → ε formation ($\Delta G^{\gamma\to\varepsilon}$) by chemistry change but also $\Delta S_{conf}^{\gamma\to\varepsilon}$ by increasing number of constiuent elements in the alloy. For increasing $\Delta S_{conf}^{\gamma\to\varepsilon}$, we decided to have 5 or 6 constituent elements in the new alloy which is along the guidance proposed by Yeh et al. [4] for having subtantial benefit of high entropy of mixing in an alloy.

The tunning of $\Delta G^{\gamma\to\varepsilon}$ is done as follows. The literature on TRIP steel [22] suggested that, Si addition in Fe—Mn matrix increases the driving force $\Delta G^{\gamma\to\varepsilon}$ for ε-phase formation whereas Ni addition decreases it. Moreover, recent work by Liu et al. [25] showed increased tendency of ε-phase formation with increase in the Co and Cr content in Fe-Mn-Ni system. In our alloy design, we varied the amount of Si in Fe-Mn-Co-Cr matrix to see the effect on $\Delta G^{\gamma\to\varepsilon}$ at room temperature since Si is the strong ε stabilizer [12]. While doing that we fixed Mn and Co content to 20 at. %, and Cr to 15 at. % to further assist in increasing the ε stability [25]. The CALPHAD-based approch was used to estimate the effects of Si addition on $\Delta G^{\gamma\to\varepsilon}$ in $Fe_{45-x}Mn_{20}Co_{20}Cr_{15}Si_x$ system using Thermo-Calc TCHEA2 database.

Fig. 3 (a) show the effect of Si addition on $\Delta G^{\gamma\to\varepsilon}$ at room temperature and it clearly shows that the absolute value of $\Delta G^{\gamma\to\varepsilon}$ increased with Si whereas negative sign indicated the higher stability of ε-phase. However, higher content of Cr with Si always increases the risk of hard and brittle σ-phase formation in the alloy system. Thus, we also estimated the Gibbs free energy of σ-phase formation ($\Delta G^{\gamma\to\sigma}$) at room temperature as a function of Si content in $Fe_{45-x}Mn_{20}Co_{20}Cr_{15}Si_x$ system and compared with the $\Delta G^{\gamma\to\varepsilon}$ values at room temperature (RT) to decide the Si amount to be added in the alloy which can suppres σ-phase formation. Fig. 3 (b) shows that $\Delta G^{\gamma\to\sigma}$ is always higher than $\Delta G^{\gamma\to\varepsilon}$ irrespective of Si content of 9 at.% thereby suggesting formation of ε-phase is favored over σ-phase with Si addition at room temperature. Further, the overall increase in (α + ε) phase field up to ~350 °C till 5 at.% is also evident from the $Fe_{45-x}Mn_{20}Co_{20}Cr_{15}Si_X$ pseudo-binary phase diagram obtained from Thermo-Calc (Fig. 3 (c)). Thus, Si addition of more than 5 at.% not only suppresses σ-phase formation but also stabilizes the (γ + ε) phase field till 350 °C and hence we selected 5 at.% Si to be added in $Fe_{45-x}Mn_{20}Co_{20}Cr_{15}Si_x$. This led down to a composition of $Fe_{40}Mn_{20}Co_{20}Cr_{15}Si_5$ for the new alloy we designed, which we termed as CS-HEA [26,27].

It is reported [26] that Al and/or Cu addition makes the γ matrix more stable in Fe-Mn-Ni system and hence moves away from the TRIP effect (Fig. 2(b)). However, it is expected that synergistic addition of Cu/Al with Si would retain the γ metastability depending upon the

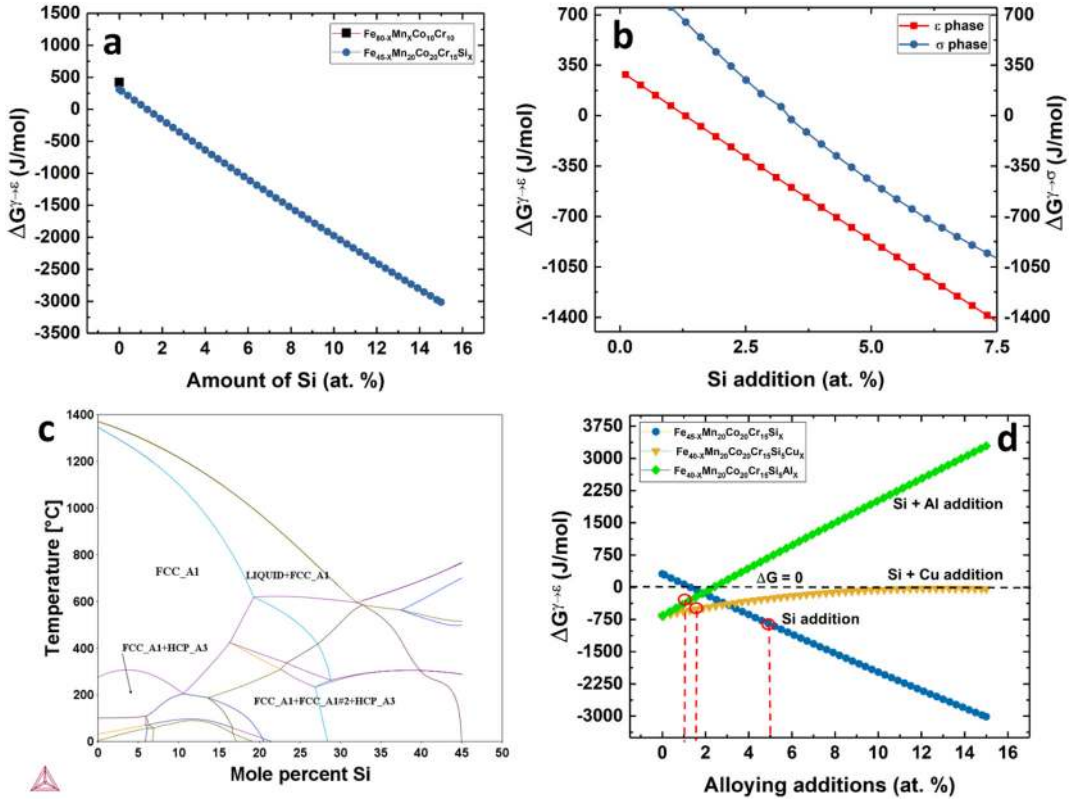

Fig. 3. Thermodynamic investigation using TCHEA2 database. (a) $\Delta G^{\gamma\rightarrow\varepsilon}$ values at room temperature plotted as a function of Si content for $Fe_{45-x}Mn_{20}Co_{20}Cr_{15}Si_x$ alloy system, (b) a comparison plot for $\Delta G^{\gamma\rightarrow\varepsilon}$ and $\Delta G^{\gamma\rightarrow\sigma}$ values at room temperature as a function of Si content, (c) a pseudo-binary $Fe_{45-x}Mn_{20}Co_{20}Cr_{15}Si_x$ alloy phase diagram, and (d) $\Delta G^{\gamma\rightarrow\varepsilon}$ values at room temperature plotted as a function of Al and Cu content in $Fe_{40-x}Mn_{20}Co_{20}Cr_{15}Si_5Y_x$ alloy system.

competing effects of Cu/Al additions on $\Delta G^{\gamma\rightarrow\varepsilon}$. Moreover, addition of one more element in $Fe_{40}Mn_{20}Co_{20}Cr_{15}Si_5$ alloy would increase the $\Delta S^{\gamma\rightarrow\varepsilon}_{conf}$ and hence can provide with more entropy effect. Thus, CALPHAD based ThermoCalc software (TCHEA2 database) were used to predict the $\Delta G^{\gamma\rightarrow\varepsilon}$ values as a function of Al or Cu addition in $Fe_{40-x}Mn_{20}Co_{20}Cr_{15}Si_5Y_x$ (where Y = Al or Cu) matrix as shown in Fig. 3 (d). Al was found to dominate in stabilizing the γ-phase beyond 2 at.% whereas Cu showed marginal increase in $\Delta G^{\gamma\rightarrow\varepsilon}$ values till 4 at.%, beyond which the variation becomes sluggish (yellow and green lines in Fig. 3 (d)). Hence, we selected 1 at.% Al and 1.5 at.% Cu, respectively, along with 5 at.% Si as minor additions in $Fe_{40-x}Mn_{20}Co_{20}Cr_{15}Si_x$ to see the effect on overall phase metastability and tensile behavior as compared with CS-HEA [12–15].

It is clear from Fig. 3 (a-d) that, CS-HEA has the most negative $\Delta G^{\gamma\rightarrow\varepsilon}$ as compared to $Fe_{39}Mn_{20}Co_{20}Cr_{15}Si_5Al_1$ (Al-HEA) and $Fe_{38.5}Mn_{20}Co_{20}Cr_{15}Si_5Cu_{1.5}$ (Cu-HEA) suggesting that it is the most metastable HEA among them. Higher metastability in CS-HEA is thus expected to provide higher flexibility in phase evolution as well as deformation accomodation as discussed earlier. All these thermodynamic predictions were verified for all these new HEA compositions after doing FSP. FSP was chosen to have sysnergistic action of strain rate and temperature to verify flexible phase evolution for a given alloy chemistry [12–15].

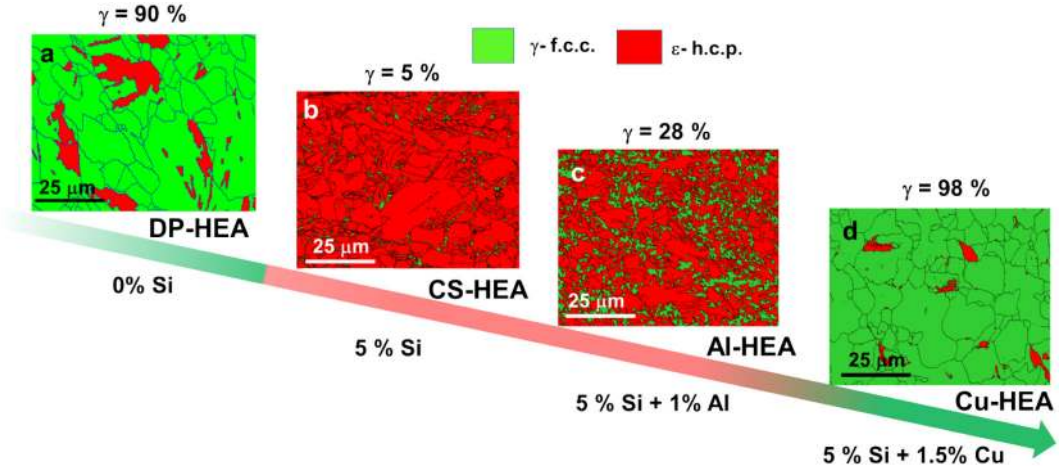

Fig. 4. Design path for microstructurally flexible HEAs as shown by EBSD phase maps in (a) DP-HEA [10], (b) CS-HEA, (c) Al-HEA, and (d) Cu-HEA.

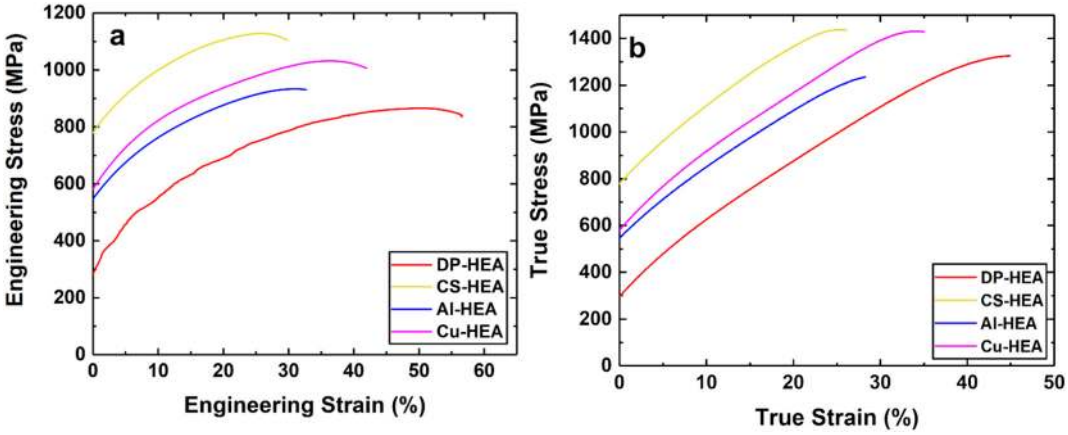

Fig. 5. Deformation behavior of flexible HEAs: (a) engineering stress-strain curves for all TRIP HEAs in S350 condition during room-temperature tensile deformation at strain rate of 10^{-3} s^{-1}, and (b) true stress-true strain curves for all TRIP HEAs in S350 condition during room-temperature tensile deformation at strain rate of 10^{-3} s^{-1}.

The detail experimental results are discussed in subsequent sections to provide evidence of microstructural flexibility.

3.3. Responsive phase evolution and stress- strain response in designed HEAs

Fig. 4 captures the overall design path and resultant microstructural evolution in microstructurally flexible HEAs. All these HEAs were melted under similar casting conditions and subsequently friction stir processed at a tool rotation rate of 350 rotations per minute (S350); as predicted from the Thermo-Calc analysis, Si addition makes the Fe-Mn-Co-Cr matrix extremely unstable and hence most of the Si containing HEAs except Cu-HEA showed very higher fraction of ε-phase in S350 condition, which makes them different from dual phase HEA (DP-HEA), which displayed γ dominance in the microstructure under similar processing condition (Fig. 4 (a-d)).

The systematic variation in the alloy compositions with the combined additions of 1 at.% Al + 5 at. % Si (Fig. 4 (c)) and 1.5 at.%

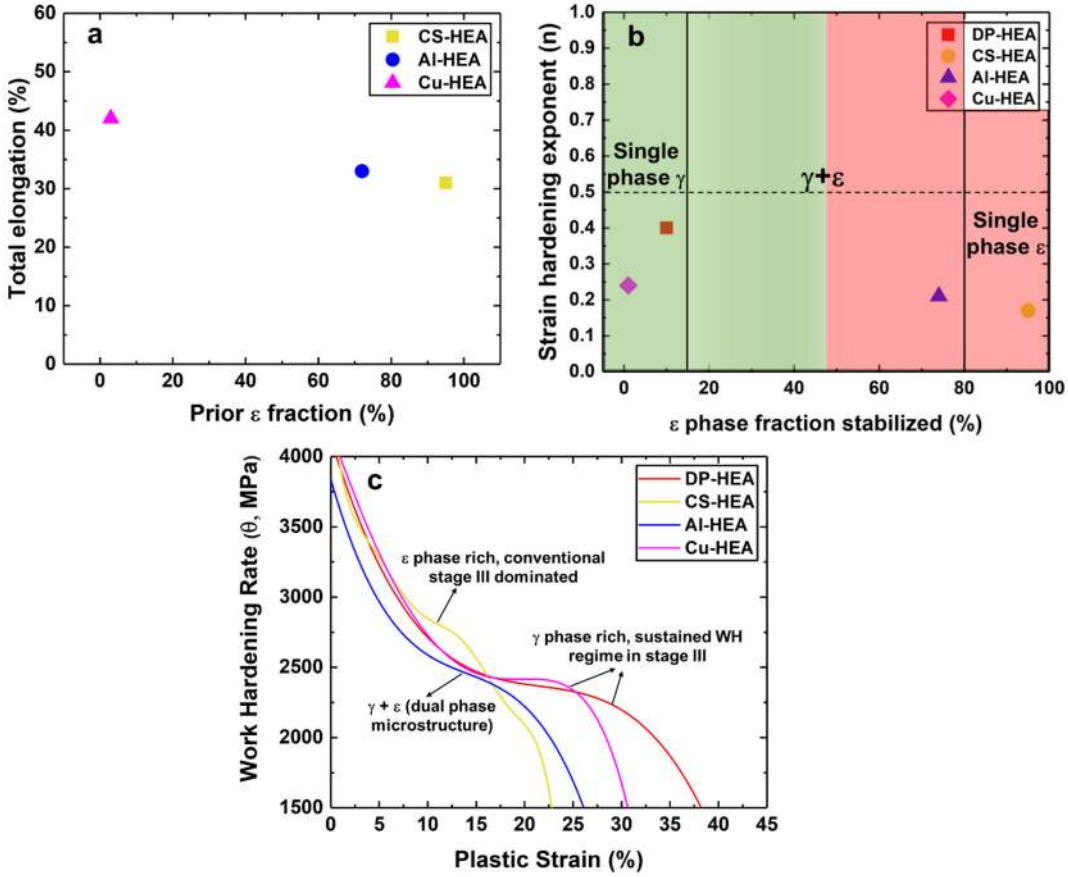

Fig. 6. (a) Effect of prior ε fraction on total elongation in various TRIP HEAs, (b) strain hardening exponent (n) vs ε fraction stabilized after processing for flexible HEAs (maximum standard error in the measurement of ductility (a) and strain hardening exponents (b) are within ±6% at 95% confidence level.), and (c) work hardening rate vs. plastic strain (%) for all HEAs in S350 condition. (HEA: high entropy alloy).

Cu + 5 at. % Si (Fig. 4 (d)) displayed drastic variation in phase evolution after FSP in comparison with the addition of 5 at.% Si alone (Fig. 4 (b)) [12–15]. The results are in accordance with the predictions made by Thermo-Calc (Fig. 3 (d)) suggesting increased γ stability with Al and Cu. Along with phase evolution, the average grain sizes obtained for these MF-HEAs were fine (varying in the range of 0.8–2.5 μm, [12–15]) in comparison with DP-HEA having an average grain size of 6.5 μm. The microstructural flexibility provides easy pathways to engineer the microstructure of HEAs to attain not only required ε/γ fractions but also obtain desired grain size and morphology for improved mechanical performance of the material [10–15,21–24].

Understanding the significance of flexible microstructural evolution in HEAs on their deformation behavior is quite important. Fig. 5 (a) shows engineering stress-engineering strain curves for these metastable HEAs with respect to chemistry based flexibility. In order to highlight substantial difference in the strain hardening behavior of all these TRIP HEAs under similar FSP processing at 350 RPM, true stress-true strain curves are shown in Fig. 5 (b). The massive effect of Si addition is evident which not only improved the yield strength (YS) but also maintained the high strength-ductility combination in MF-HEAs in comparison with the HEAs without Si (yellow and red curves in Fig. 5 (a)). Fig. 5 (a) also makes it clear that, within Si containing TRIP HEAs, CS-HEA being most flexible, showed the highest work hardening rate (WHR) in comparison with the less flexible Al-HEA with similar uniform elongation of ~30%. However, the least flexible Cu-HEA also showed relatively lower WHR with improved ductility. It is also important to note that all these HEAs exhibited almost similar elongation despite different work hardenability. Thus, it is important to investigate the deformation mechanisms in the ε or γ phases.

3.4. Deformation mechanisms

As mentioned in the previous sections, two microstructural variants were selected for studying the deformation mechanisms. Earlier work [10–12] on TRIP HEAs showed that higher ε fraction (f_ε) and lower grain size (d) hinders the $\gamma \rightarrow \varepsilon$ transformation and thus should increase the retained γ-phase fraction after deformation to failure for a given alloy chemistry. Also, Li et al. [10] mentioned that ε martensite is harder than the γ-phase and hence it is expected that the material will exhibit typical limited plasticity behavior if the microstructure is near single ε-phase (conventional h.c.p. type). It was interesting to see that these metastable HEAs (mainly Cu-HEA and CS-HEA) showed almost similar ductility (total elongation) in spite of having dominance of either softer γ or harder ε-phase (Fig. 6 (a)). Further, it is noted that, the inherent ductile nature of these alloys can also be confirmed by having strain hardening exponent (n) values ranging from 0.2–0.4 (Fig. 6 (b)) irrespective of the dominance of single phase or dual phase microstructure. This may be attributed to the tunable work hardening ability in these materials which is based on the activation of preferential deformation modes decided by the dominant phase [10–15,28,29].

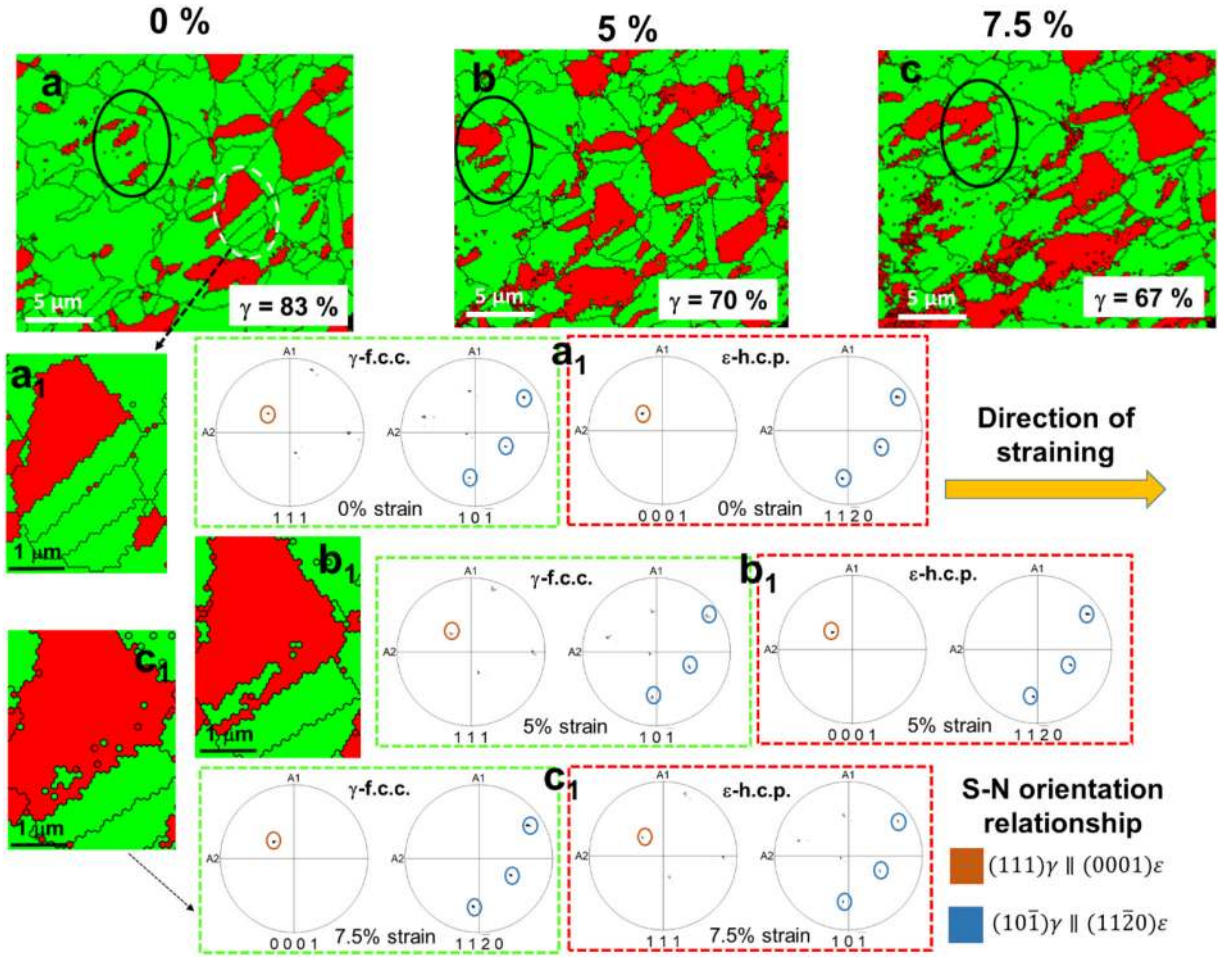

Fig. 7. EBSD phase maps for γ dominated microstructure in, (a) as-FSP condition, (b) after 5% strain, and (c) after 7.5% strain. (a_1) EBSD phase for a selected grain of 0% deformed specimen along with the discrete pole figures of γ-f.c.c. and ε-h.c.p. phases corresponding to these grains, (b_1) EBSD phase for a selected grain of 5% deformed specimen along with the discrete pole figures of γ-f.c.c. and ε-h.c.p. phases corresponding to these grains, and (c_1) EBSD phase for a selected grain of 7.5% deformed specimen along with the discrete pole figures of γ-f.c.c. and ε-h.c.p. phases corresponding to these grains. (EBSD: electron back scattered diffraction, IPF: inverse pole figure; HEA: high entropy alloy).

Fig. 6 (c) shows the WH curves for all these HEAs in S350 condition. It can be seen that, γ dominated microstructure appears to accommodate strain primarily with transformation induced plasticity due to sustained WH over a wide plastic strain range of 15–35%. On the other hand, ε dominated microstructure appears to deform due to synergistic action of non-basal slip and twinning and is depicted by the traditionally drooping WH rate in stage III for CS-HEA in Fig. 6 (c). Dual phase microstructure however work hardens with classical back stress strengthening as explained in most of the research done on TRIP HEAs/steels till date and is suggested by the gradual decrease in the WH rate over strain range of 12.5–20% (blue line in Fig. 6 (c)). To confirm this, a detail microstructural investigation was carried out with both the microstructural variants.

A specimen with γ-phase dominated microstructure (83% γ-phase) was interrupted at 5% and 7.5% plastic strain and the microstructure was characterized at the same locations (same grains). Fig. 7 (a-c) capture γ → ε transformation showing an increase in ε-phase fraction from 17 to 33% after 7.5% strain. This progressive increase in the ε-phase fraction (and corresponding decrease in γ phase fraction) with strain suggests that transformation induced plasticity is a primary strain accommodation mechanism in the material (Fig. 7 (a-c)). Moreover, detail EBSD analysis was carried out of a selected γ/ε grain pair as shown in 7 (b) to capture the preferred orientation relationship among them. The nucleation of ε-phase occurred at the γ/ε interphase boundary with an orientation relationship (OR) close to Shoji-Nishiyama (S—N) OR consisting of $(111)\gamma \parallel (0001)\varepsilon$ and $(10\bar{1})\gamma \parallel (11\bar{2}0)\varepsilon$ as shown by the discrete pole figures in Fig. 7 (a_1-c_1).

Herrera et al. [30] made similar observations wherein they found profound existence of S—N OR among γ-austenite and ε-martensite phases in Mn containing TRIP steel [30]. It was further noted that, the OR after deformation was similar to the OR of the pre-existing γ/ε phase boundary as confirmed from the discrete pole figures of the 0% deformed specimen with 5% deformed specimen (Fig. 7 (a_1-b_1)). Moreover, the growth of the ε martensite phase also occurred by confining to the same OR with γ-phase upon incremental straining to 7.5% (Fig. 7 (a_1-c_1)). Thus, the main strain accommodation mechanism in γ dominated HEAs is TRIP and it is prevalent in grains exhibiting S—N OR among γ/ε phases.

The microstructure containing more than 90% ε-phase is not explored before since obtaining such a large fraction of ε-phase with fine grain size after thermo-mechanical processing was not feasible with conventional TRIP steels or HEAs. Microstructural flexibility provided an opportunity to explore this unexplored domain in TRIP HEAs by giving fine grained microstructure with 95% ε-phase for CS-HEA after FSP. Fig. 8 captures the overall deformation response of CS-HEA in S350 condition after complete tensile deformation. As the sample was heavily deformed with ~95% prior ε-phase fraction, it was important to understand the deformation accommodation of almost 32% in the sample. A detailed TEM based OIM-PED study of the deformed specimen revealed the microstructure to be mainly ε dominant as shown in the phase map (Fig. 8 a_3 and b_3) similar to that of SEM-EBSD (Fig. 2 (c_3). The interesting information obtained from conventional bright field TEM and PED (Fig. 8 (a – c)) was the presence of both nano-size ε plates and twins co-existing. Fig. 8 (a-c) show the presence of ε plates along with

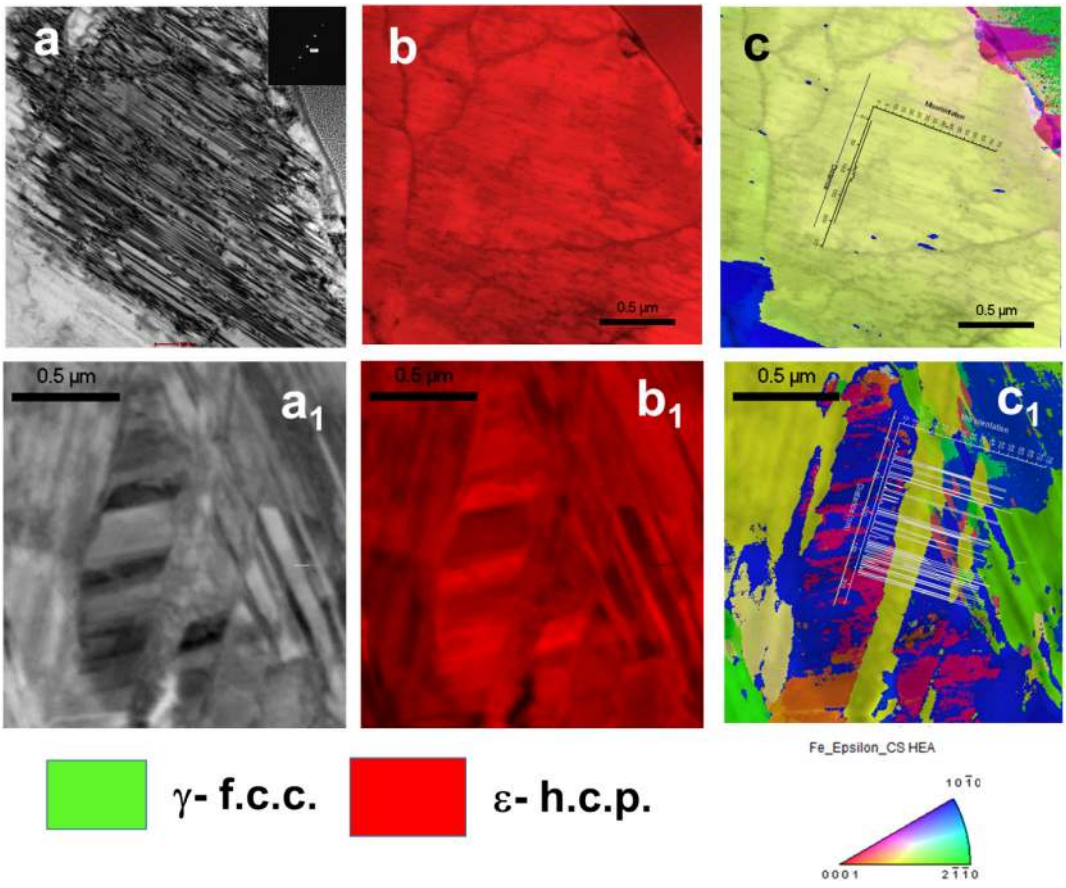

Fig. 8. TEM based PED maps for FSP CS HEA after complete tensile deformation. (a) Bright field TEM image showing the presence of nano sized ε plates and subgrains. (b) PED phase map region shown in Fig. 8 (a) showing dominance of ε-phase, (c) IPF map with misorientation map superimposed for the region shown in Fig. 8 (a), (a_1) bright field TEM image showing presence of nano-twins in different grains, (b_1) PED phase map for the region shown in Fig. 8 (a_1), (c_1) IPF map for the region shown in Fig. 8 (a_1) with misorientation map superimposed. (TEM: Transmission electron microscopy, PED: precision electron diffraction, IPF: inverse pole figure; HEA: high entropy alloy).

subgrains within the larger grain of ε-phase whereas Fig. 8 (a_1-c_1) show formation of nano twins within ε-phase.

Bu et al. [31] already reported activation of <c + a> slip in metastable HEAs within ε-phase having c/a ratio of 1.616 which is also in accordance with our recent work [32] with in situ neutron diffraction studies on CS-HEA confirming non basal activity by concurrent reduction of c/a ratio of ε-h.c.p. phase from 1.619 to 1.588 [32,33]. Thus, lower c/a ratio promotes early activation of non-basal activity in ε-phase of CS-HEA. It is known that, non-basal activity at room temperature promotes dynamic recovery in hcp materials which we think is the driving force for the formation of ε-phase nano-plates after complete tensile deformation. Formation of nano-plates is the result of minimized strain energy since plate shape provides less misfit during nucleation in the parent matrix of similar orientation [20–24]. Misorientation analysis along these plates show no distinct peaks and hence all those nano-plates have similar orientation as that of parent ε grain suggesting them to be sub grains. Further, the periodic breaks in the WHR curve for CS-HEA at the strain levels of 10% and 16% shows (yellow curve in Fig. 6 (c)) change in slope which in HCP materials is associated with the dynamic recovery and sub-grain formation [31–34].

Twinning in h.c.p. phase, however, is dependent on c/a ratio and grain size. Due to extremely fine grain size and low c/a ratio of S350 CS-HEA specimen, twinning became difficult in ε-phase and hence it gets activated at higher stresses and later stage of deformation. Figs. 8 (a_1–b_2) shows the presence of ε nano-twins in different grains as confirmed by OIM and misorientation map showing a misorientation of 58° (Figs. 8 (c_2)). This type of special boundaries corresponding to 58° misorientation points towards typical {10.1} contraction twins in h.c.p. alloys. In short, activation of non-basal activity assisted nano-plate formation at early stages and nano-twinning at later stages accommodated the deformation in ε dominated microstructure which provided a good ductility of ~32% at room temperature [34–36].

3.5. Microstructurally flexible HEAs: overall comparison of mechanical response with TRIP HEAs and steels

The recent work of Li et al. [10] on design of non-equiatomic HEAs opened a new path to obtain strong and ductile HEAs. However, these HEAs exhibit poor yield strength (YS). As far as all structural applications are concerned, low YS materials have lower usability than high YS materials using the criterion of safety; hence the need to increase the YS of these TRIP HEAs without compromising their inherent qualities. Metastability-based design of flexible HEAs overcomes this difficulty by obtaining a range of YS values from 600 to 900 MPa (Fig. 4 (a)) with sustained work hardenability. However, processing methodology along with alloy design strategy led to this excellent outcome of properties in our HEAs. Fig. 9 (a) displays the conventional processing method adopted in processing of TRIP HEAs in earlier work [10,11] along with the objective behind each step. Fig. 9 (b) shows the processing path we followed with the same objectives in mind. Figs. 2 (a-b) clearly confirm that we could achieve the same microstructural engineering of TRIP HEAs in a much simpler way than conventional processing (for a particular specimen dimension), due to the unique nature of FSP that involved simultaneous control on grain refinement, phase evolution and chemical homogeneity [12–15].

Fig. 9 (b) displays the strength-ductility index ((true UTS-YS) × ductility) for all TRIP HEAs reported so far plotted with the amount of ε obtained after FSP. It is also important to note that,

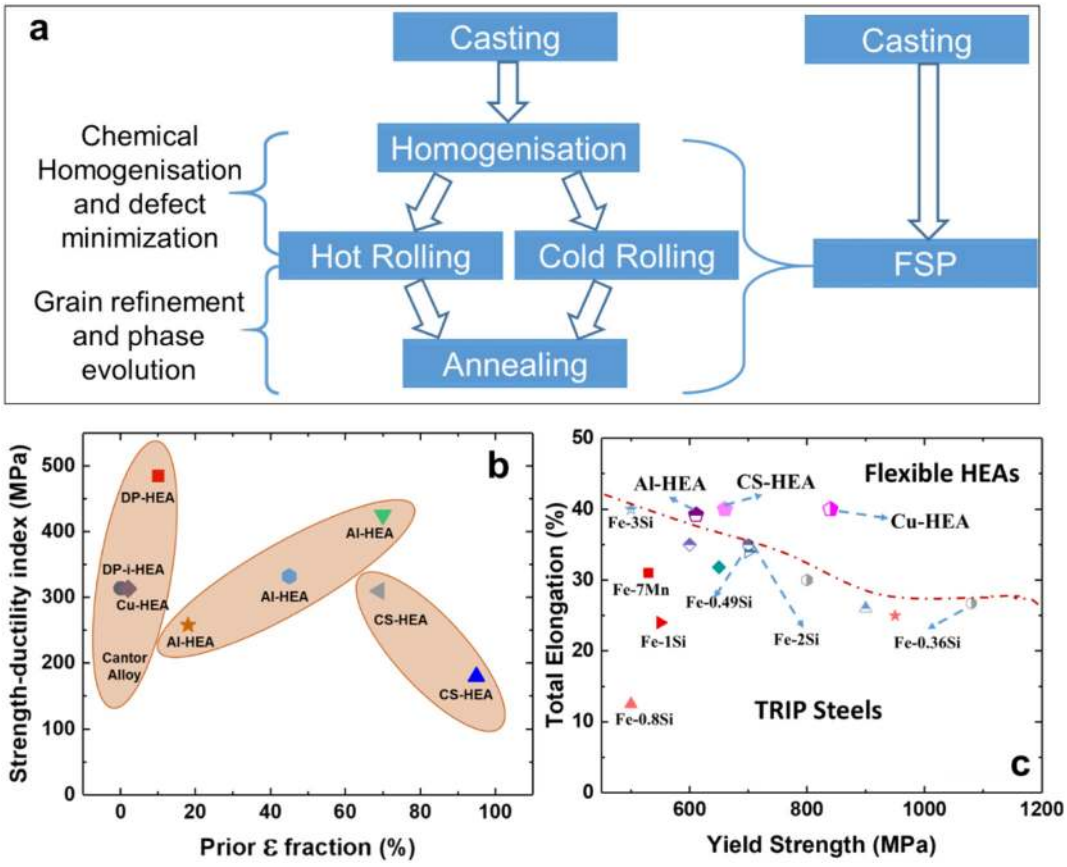

Fig. 9. TRIP HEAs overview: (a) Processing methodology used for microstructural engineering of TRIP HEAs. (b) Strength-ductility index for all TRIP HEAs plotted with the stabilized ε fraction after FSP [10–15]. (c) Total elongation vs. yield strength plot for flexible HEAs in comparison with advanced Si-containing TRIP steels [37–44]. (TRIP: transformation induced plasticity, DP: dual phase, HEA: high entropy alloy).

flexibility based alloy design helped to explore the overall ε-phase fraction range with multiple deformation modes. Moreover, MF based alloy design opened an untouched microstructural regime of having almost ~95% ε-phase which not only showed exceptional strength but comparable ductility by twinning and nan-basal slip activity within ε-phase [14,30,31]. Thus, these TRIP HEAs are not only responsive for the phase stability but also can select the deformation accommodation mechanisms for attaining higher strength and ductility based on dominant phase in the microstructure.

Fig. 9 (c) compares YS and total elongation of flexible HEAs [10–14] with the Si-containing advanced TRIP steels [37–47]. The plot includes data for steels and HEAs having YS more than 500 MPa, since YS below that is not attractive from a design perspective [48]. The flexible HEAs open a new YS and ductility domain (Fig. 9 (c)) wherein they exhibit higher YS with good ductility as desired for many structural applications, particularly for energy absorbing structures.

4. Summary

Here we presented alloy design and processing approach for metastable non-equiatomic TRIP HEAs that resulted in excellent mechanical properties. Along with conventional 3d transition metal elements, a non-transition element Si was introduced into the Fe-Mn-Co-Cr matrix, which drastically altered γ stability at room temperature. Coupled with Si addition, FSP was used as a microstructural engineering tool, which, due to its unique nature, triggered responsive phase evolution along with grain refinement. This responsive phase evolution stabilized either thermodynamically stable γ or unstable ε-phase because of synergistic actions of chemistry and processing, which have been termed as microstructural flexibility. This approach heads to significant improvement in YS of initially reported TRIP HEAs while retaining higher strength-ductility combinations.

Further, we observed that tuning the γ stability by either processing or annealing of γ stabilizers (Cu or Al) containing Fe-Mn-Co-Cr-Si can produce a range of γ or ε dominated microstructures with engineered work hardenability. An interesting observation was that, irrespective of the dominance of either γ or ε-phase in the starting microstructure, ductility was retained because of the selective operation of deformation mechanisms decided by the dominant phase.

Data availability statement

The raw/processed data required to reproduce these findings cannot be shared at this time as the data also forms part of an ongoing study.

Declaration of Competing Interest

The authors have no conflict of interest.

Acknowledgments

The work was performed under a cooperative agreement between the Army Research Laboratory and the University of North Texas (W911NF-19-2-0011). The authors are thankful to the Materials Research Facility for providing access to the microscopy facilities at the University of North Texas.

References

[1] H. Kim, W.D. Suh, J.N. Kim, Fe–Al–Mn–C lightweight structural alloys: a review on the microstructures and mechanical properties, Sci. Technol. Adv. Mater. 14 (2013) 014205.
[2] L. Wang, M. Makhlouf, D. Apelian, Aluminium die casting alloys: alloy composition, microstructure, and properties-performance relationships, Int. Mater. Rev. 40 (1995) 221–238.
[3] B.B. He, B. Hu, H.W. Yen, G.J. Cheng, Z.K. Wang, H.W. Luo, M.X. Huang, High dislocation density–induced large ductility in deformed and partitioned steels, Science 357 (2017) 1029–1032.
[4] J.W. Yeh, S.K. Chen, S. Lin, J.Y. Gan, T.S. Chin, T.T. Shun, C.H. Tsau, S.Y. Chang, Nanostructured high entropy alloys with multiple component elements: novel alloy design concepts and outcomes, Adv. Eng. Mater. 6 (2004) 299–303.
[5] B. Cantor, I.T.H. Chang, P. Knight, A.J.B. Vincent, Microstructural development in equiatomic multicomponent alloys, Mater. Sci. Eng. A 375 (2004) 213–218.
[6] D.B. Miracle, O.N. Senkov, A critical review of high entropy alloys and related concepts, Acta Mater. 122 (2017) 448–511.
[7] B. Gludovatz, A. Hohenwarter, D. Catoor, H.E. Chnag, P.E. George, O.R. Ritchie, A fracture resistant high entropy alloy for cryogenic applications, Science 345 (2014) 1153–1158.
[8] L.J. Santodonato, Y. Zhang, M. Feygenson, C.M. Parish, M.C. Gao, R.J.K. Weber, J.C. Neuefeind, Z. Tang, P.K. Liaw, Deviation from high-entropy configurations in the atomic distributions of a multi-principal-element alloy, Nature Comm. 6 (2015) 5964.
[9] M.A. Hemphill, T. Yuan, G.Y. Wang, J.W. Yeh, C.W. Tsai, A. Chuang, P.K. Liaw, Fatigue behavior of Al0.5CoCrCuFeNi high entropy alloys, Acta Mater. 60 (2012) 5723–5734.
[10] Z. Li, K.G. Pradeep, Y. Deng, D. Raabe, C.C. Tasan, Metastable high-entropy dual-phase alloys overcome the strength-ductility trade-off, Nature 534 (2016) 227–230.
[11] Z. Li, C.C. Tasan, H. Springer, B. Gault, D. Raabe, Interstitial atoms enable joint twinning and transformation induced plasticity in strong and ductile high-entropy alloys, Sci. Rep. 7 (2017) 40704.
[12] S.S. Nene, K. Liu, M. Frank, R.S. Mishra, R.E. Brennan, K. Cho, Z. Li, D. Raabe, Enhanced strengh and ductility in friction stir processed engineered high entropy alloy, Sci. Rep. 7 (2017) 16167.
[13] S.S. Nene, M. Frank, K. Liu, S. Sinha, R.S. Mishra, B. McWilliams, K.C. Cho, Reversed strength-ductility relationship in microstructurally flexible high entropy alloy, Scr. Mater. 154 (2018) 163–167.
[14] S. Nene, M. Frank, K. Liu, S. Sinha, R.S. Mishra, B. McWilliams, K.C. Cho, Unexpected strength-ductility response of an annealed metastable phase high entropy alloy, Appl. Mater. Today 13 (2018) 198–206.
[15] S.S. Nene, M. Frank, K. Liu, S. Sinha, R.S. Mishra, B. McWilliams, K.C. Cho, Corrosion resistant high entropy alloy with high strength and ductility, Scr. Mater. 166 (2019) 168–172.
[16] S.F. Liu, Y. Wu, H.T. Wang, W.T. Lin, Y.Y. Shang, J.B. Liu, K. An, X.J. Liu, H. Wang, Z.P. Lu, Transformation-reinforced high-entropy alloys with superior mechanical properties via tailoring stacking fault energy, J. Alloys Compd. 792 (2019) 444–455.
[17] L. Zhao, N. Park, Y. Tian, A. Shibata, N. Tsuji, Combination of dynamic transformation and dynamic recrystallization for realizing ultrafine-grained steels with superior mechanical properties, Sci. Rep. 6 (2016) 39127.
[18] R. Xiong, H. Peng, H. Si, W. Zhang, Y. Wen, Thermodynamic calculation of stacking fault energy of the Fe-Mn-Si-C high manganese steels, Mater. Sci. Eng. A 598 (2014) 376–386.
[19] C. Herrera, D. Pong, D. Rabbe, Design of a novel Mn-based 1GPa duplex stainless TRIP steel with 60% ductility by reduction of austenite stability, Acta Mater. 59 (2011) 4653–4664.
[20] B.S. Murty, J.W. Yeh, S. Rangnathan, High Entropy Alloys, Butterworth Heinemann Publications, London NW1 7BY, UK, 2014.
[21] D.A. Porter, K.E. Esterling, M.Y. Sherif, Phase Transformations in Metals and Alloys (Third Edition), CRC Press, Boca Raton FL, USA, 2009.
[22] E.I. Galindo-Nava, P.E.J. Rivera-Díaz-del-Castillo, Understanding martensite and twin formation in austenitic steels: a model describing TRIP and TWIP effects, Acta Mater. 128 (2017) 120–134.
[23] G.B. Olson, M. Cohen, A general mechanism of martensitic nucleation: Part I. General concepts and the FCC → HCP transformation, Metall. Trans. A. 7 (1976) 1897–1904.
[24] W. Lu, C.H. Liebscher, G. Dehm, D. Raabe, Z. Li, Bidirectional transformation enables hierarchical nanolaminate dual-phase high-entropy alloys, Adv. Mater. 1804727 (2018).
[25] Z. Li, D. Raabe, Strong and Ductile Non-equiatomic High-Entropy Alloys: Design, Processing, Microstructure, and Mechanical Properties, JOM 69 (2017) 2099–2106.
[26] S.T. Pisarik, D.C. Van Aken, Thermodynamic driving force of the γ → ε transformation and resulting M_S temperature in high-Mn steels, Metall. Mater. Trans. A. 47 (2016) 1009–1018.
[27] F. Trichter, A study on γ → ε phase transformation in Fe-Mn alloys induced by high pressure and plastic deformation, Scr. Metall. 12 (1978) 431–434.
[28] M Wang, Z. Li, D. Raabe, In-situ SEM observation of phase transformation and twinning mechanisms in an interstitial high-entropy alloy, Acta Mater. 147 (2018) 236–246.
[29] M. Calcagnotto, D. Ponge, E. Demir, D. Raabe, Orientation gradients and geometrically necessary dislocations in ultrafine grained dual-phase steels studied by 2D and 3D EBSD, Mater. Sci. Eng. A 527 (2010) 2738–2746.
[30] C. Herrera, D. Ponge, D. Raabe, Design of a novel Mn-based 1 GPa duplex stainless TRIP steel with 60% ductility by a reduction of austenite stability, Acta Mater. 59 (2011) 4653–4664.
[31] Y. Bu, Z. Li, J. Liu, H. Wang, D. Raabe, W. Yang, Nonbasal slip systems enable a strong and ductile hexagonal-close-packed high-entropy phase, Phys. Rev. Lett. 122 (2019) 075502.
[32] M. Frank, Y. Chen, S.S. Nene, S. Sinha, K. Liu, K. An, R.S. Mishra, Investigating the deformation mechanisms of a highly metastable high entropy alloy using in-situ neutron diffraction, Mater. Today Comm 23 (2020) 100858.
[33] S. Sinha, S.S. Nene, M. Frank, K. Liu, R.A. Lebensohn, R.S. Mishra, Deformation mechanisms and ductile fracture characteristics of a friction stir processed transformative high entropy alloy, Acta Mater. 184 (2020) 164–178.

[34] Y. Estrin, S.S. Nene, B.P. Kashyap, N. Prabhu, T. Al-Samman, New hot rolled Mg-4Li-1Ca alloy: a potential candidate for automotive and biodegradable implant applications, Mater. Lett. 173 (2016) 252–256.
[35] S. Sinha, N.P. Gurao, In situ electron backscatter diffraction study of twinning in commercially pure titanium during tension-compression deformation and annealing, Mater. Des. 116 (2017) 686–693.
[36] J. Shi, X. Sun, M. Wang, W. Hui, H. Dong, W. Cao, Enhanced work-hardening behavior and mechanical properties in ultrafine-grained steels with large-fractioned metastable austenite, Scr. Metall. 63 (2010) 815–818.
[37] P. Xie, M. Han, C.L. Wu, Y.Q. Yin, K. Zhu, R.H. Shen, J.H. Chen, A high-performance TRIP steel enhanced by ultrafine grains and hardening precipitates, Mater. Des. 127 (2017) 1–7.
[38] B.B. He, B.M. Huang, S.H. He, Y. Qia, H.W. Yen, M.X. Huang, Increasing yield strength of medium Mn steel by engineering multiple strengthening defects, Mater. Sci. Eng. A 724 (2018) 11–16.
[39] D. Raabe, D. Ponge, O. Dmitrieva, B. Sander, Nanoprecipitate-hardened 1.5 GPa steels with unexpected high ductility, Scr. Metall. 60 (2009) 1141–1144.
[40] I.D. Choi, M. Bruce, S.J. Kim, C.G. Lee, S.H. Park, D.K. Matlock, J.G. Speer, Deformation behavior of low carbon trip sheet steels at high strain rates, ISIL Intl. 42 (2002) 1483–1489.
[41] M. Mukherjee, O. Mohanty, S. Hashimoto, T. Hojo, K. Sugimoto, Strain-induced transformation behaviour of retained austenite and tensile properties of trip-aided steels with different matrix microstructure, ISIL Intl. 46 (2006) 316–324.
[42] K. Sugimoto, M. Kobayashi, S. Hashimoto, Ductility and strain-induced transformation In a high-strength transformation-induced plasticity-aided dual-phase steel, Metall. Trans. A. 23 (1992) 3085–3091.
[43] S.C. Baik, S. Kim, Y. Jin, O. Kwon, Effects of alloying elements on mechanical properties and phase transformation of cold rolled trip steel sheets, ISIL Intl. 41 (2001) 290–297.
[44] Z.C. Li, R.D.K. Misra, Z.H. Cai, H.X. Li, H. Ding, Mechanical properties and deformation behavior in hot-rolled 0.2C-1.5/3Al-8.5Mn-Fe TRIP steel: the discontinuous TRIP effect, Mater. Sci. Eng. A 673 (2016) 63–72.
[45] D.P. Escobar, S.S. Ferreira de Dafé, D.B. Santos, Martensite reversion and texture formation in 17Mn-0.06C TRIP/TWIP steel after hot cold rolling and annealing, J. Mater. Res. Techol. 4 (2015) 162–170.
[46] G. Frommeyer, U. Brüx, P. Neumann, Supra-ductile and high-strength manganese-trip/twip steels for high energy absorption purposes, ISIL Intl. 43 (2003) 438–446.
[47] P.J. Jacques, E. Girault, Ph. Harlet, F. Delannay, The developments of cold-rolled trip-assisted multiphase steels. low silicon trip-assisted multiphase steels, ISIL Intl. 41 (2001) 1061–1067.
[48] J. Shigley, C. Mischke, Standard Handbook of Machine Design, McGraw-Hill, 1986 2–15.